Interplay between structural scales and fracture process zone: experimental and numerical analysis on paper as a model material

François Villette, Frédéric Dufour, Julien Baroth, Sabine Rolland du Roscoat, Jean-Francis Bloch

To cite this version:

François Villette, Frédéric Dufour, Julien Baroth, Sabine Rolland du Roscoat, Jean-Francis Bloch. Interplay between structural scales and fracture process zone: experimental and numerical analysis on paper as a model material. Acta Mechanica, 2023, 10.1007/s00707-023-03576-5 . hal-04145052

HAL Id: hal-04145052
https://hal.science/hal-04145052v1

Submitted on 28 Jun 2023

Interplay between structural scales and Fracture Process Zone: experimental and numerical analysis on paper as a model material

François VILLETTE[a], Frédéric DUFOUR*[a], Julien BAROTH[a], Sabine ROLLAND DU ROSCOAT[a], Jean-Francis BLOCH[a]

[a]3SR, UMR 5521, Univ. Grenoble Alpes, CNRS, Grenoble-INP[1], 38000, Grenoble, France

***Corresponding author:** Frédéric DUFOUR (Email: frederic.dufour@3sr-grenoble.fr)

Abstract:

This work deals with fracture mechanisms in quasi-brittle materials, focusing on the characterization of the Fracture Process Zone (FPZ) of specimens under tensile load. Particularly, paper was used as model material. Experiments were conducted on notched and unnotched specimens. Based on an image analysis of these observations, a stochastic finite element model was developed, using both a nonlocal stress-based approach and a discretized random field modelling of the Young's modulus. The proposed methodology allowed characterizing the damage zone and the size of the FPZ, analysing the influence of the mesostructure, composed of flocs (fiber aggregates where the basis weight is larger than the average one) and antiflocs (complement of flocs). The area of the active FPZ and the normalized stress drop were linked using a surface energy dissipated in the active FPZ. The stress drop, until limiting value, increased with the width of the active FPZ. Finally, a relationship between the surface energy and the nonlocal internal length was established.

Keywords: rupture, fracture process zone, stress-based nonlocal approach, stochastic finite element method, structural scales, mesostructure

Statements and Declarations

- **Competing Interests:** there are no conflicts to declare.
- **Funding:** no additional funding was received for conducting this study.

Acknowledgements

Laboratoire 3SR is part of the LabEx Tec 21 (Investissements d'Avenir - Grant agreement n° ANR-11-LABX-0030) and of the PolyNat Carnot Institute (Investissements d'Avenir - Grant agreement no. ANR-16-CARN-0025-01).

---

[1] Institute of Engineering, Univ. Grenoble Alpes

1. Introduction

Quasi-brittle materials include a wide range of materials; such as rock, concrete, many poly-crystalline ceramics, wood or paper; highly heterogeneous due to the presence of several structural scales. The understanding and the modelling of their fracture behaviour is of a great importance in many societal issues such as strength of concrete [1], unstable rock failure [2], crack propagation into paper sheet [3] or composite materials [4]. Induced by various heterogeneities, the failure process of quasi-brittle materials is characterized by the succession of apparitions, nucleations and stops of microcracks occurring surrounding the resulting macro crack tip [5], in the so-called Fracture Process Zone (FPZ). It is commonly considered that FPZ size does not depend on the structure size but is governed by the local heterogeneities' sizes. In these materials, the FPZ size is large enough with respect to the structure scale to influence its fracture behaviour. Therefore, it is of a crucial importance to develop models able to describe the fracture mechanisms from microstructure to structure scale.

Many approaches were used to model the quasi-brittle fracture, either discontinuous approaches such as cohesive crack models [6, 7], or regularized continuum-based approaches (plasticity or damage) such as gradient formulation [8, 9] or nonlocal integral models [10, 11]. An internal length is generally introduced to represent the damage occurrence over the FPZ. The internal length plays a pivotal role in these models because it governs the size of the FPZ which greatly influences the fracture energy and then, the fracture behaviour of the modelled structure. In the recent improvement of nonlocal models, efforts were made to use an evolving internal length [12], taking into account both boundary [13, 14] and stress state [15] effects, in order to better match with the experimental observations and overcome various suffering of nonlocal models such as wrong damage initiation at a geometric singularity [16, 17], attraction effect of the boundaries on the damage propagation [13] or nonphysical damage spreading after rupture. However, an intrinsic internal length still remains to correlate to characteristic lengths of the material. For some quasi-brittle materials, such as concrete, the literature states several indirect techniques in order to characterize the FPZ. Energy-based analysis was used to determine the FPZ size as the ratio between the fracture energy and the dissipated volume energy [18], both experimentally measured. Authors found that the internal length was 2.7 times larger than the maximum aggregate size. However, this relation was identified only on one concrete mix, geometry and loading configuration. Acoustic emission was also used to detect the localization of acoustic events (AE) during crack propagation and characterize the FPZ in concrete [19–21] and rock [22]. In this case, acoustic emission allowed directly measuring the FPZ size using criteria on the AE activity but without determine it location regarding the structural scales of the material. Moreover, the crack tip is not well determined using AE. Due to the complexity to link the internal length to the characteristic lengths of the material, the parameters of damage models, of which the internal length is part, are mostly identified by inverse analysis [23]. Therefore, only a direct observation of the FPZ and its interactions with the material structural scales could allow determining properly the FPZ geometrical characteristics, its evolution during fracture process and its links with the characteristic lengths of the material. The main drawback of most quasi-brittle materials is their opacity to the visible light which prevents to observe directly the FPZ development as well as the inner structural scales. Of course, X-ray imaging may be performed [24] but currently it is a very expensive test and the fast cinematic of the failure cannot be captured by tomography.

The paper material is one of the exceptions because its thinness allows revealing its structural scales by transmitted light as well as its process zone upon failure. Paper is a planar wood cellulosic fibrous material with a porous multiscale structure. The fiber scale defines the microscale of paper structure. Fibers are generally $1 - 3\ mm$ long and $15 - 40\ \mu m$ wide depending on the papermaking process and wood species. During papermaking process and due to the physico-chemical interactions between fibers, they tend to agglomerate with each other and form aggregates [25] which is the cause of the local basis weight variation on paper sheet called “formation”. Since the opacity of the paper depends on the basis weight [25], this formation can be visually observed as the spatial variation of opacity by lightening a sheet of paper by transmission. Darker regions, called “flocs”, correspond to the regions where the local basis weight is larger than the average one. In contrast, the antiflocs correspond to the regions where the local basis weight is lower than the average basis weight (light areas). The characteristic length of the formation defines the mesoscopic scale of the paper.

The literature states that the formation process influences the in-plane elastic and fracture properties of paper. Wong et al. [26] observed experimentally that the local strain were inversely proportional to the local basis weight. This result was confirmed using infrared thermographic analysis showing that the energy released due to plastic strain was concentrated in antiflocs. Alzweighi et al. [27] highlighted that the local density or local thickness had a larger impact on the local strain field than the variability of anisotropy. In a recent study, Villette et al. [28] showed using X-ray tomography and tensile tests on flocs and antiflocs that the local elastic modulus is linearly dependent on the basis weight and that flocs were thicker than antiflocs but had the same porosity. The spatial variability of elastic modulus, and then the strain localization which leads to fracture is mainly due to the thickness variability.

Paper damage mainly corresponds to the breakage of fiber-fiber bonds rather than fiber itself. These bonds breakages create the fracture process zone that extends over a few millimetres. Since the breakage of fiber bonds changes locally the light diffusion coefficient of paper, the FPZ of paper can be highlighted by direct observation of the damage by lightening the paper [29]. Literature states only measurements of the average width of the damage zone on *post-mortem* samples of high density papers. In particular, it was shown that the damage zone width was roughly 2.2 times the arithmetic mean fiber length for the tested paper sheet [30]. The process zone width can be characterized also using acoustic emission [31]. However, none of these approaches allowed following the local development of the FPZ in the material along with the spatial distribution of its structural scales, *i.e.* the interplay between structural scales and damage. Indeed, the measurement by direct observation has so far been obtained only *post-mortem* while the acoustic emission, performed during the test though, did not allow following directly the interaction of the FPZ with the structural scales. Particularly, the effect of the mesostructure of flocs on crack propagation has not been investigated.

Isaksson et al. [32] studied the crack growth in tension for low and high density papers. They found that (i) for high density papers, the fracture process was localised in a small region at the crack tip, while (ii) for low density papers, where the contrast between the low and high local basis weight is more pronounced, the fracture process was more diffused and took place at several locations. The use of a nonlocal damage model seems to be relevant in order to capture the observed mechanisms during fracture tests [31–34]. Nevertheless, the *a priori* identification of the internal length for paper is still an open question of great importance for the prediction ability of nonlocal model as well as to know which scales govern the fracture process in paper. Krasnoshlyk et al. [35] found that, for low density papers, the internal length of the nonlocal damage model was determined by the size of the largest antiflocs. Isaksson and Hägglund [34] reported that the internal length seems to be also related to the mean degree of fiber-fiber bonds per fiber. Then, the governing characteristic length seems to be more related to the fiber network structure at micro and mesoscales than to fibers’ geometry taken alone [35].

Therefore, in this original contribution is proposed to determine the geometrical characteristics of the FPZ and their evolution during the fracture process of paper using a combined approach including both experimental and numerical analysis. The modelling of tensile fracture tests of heterogeneous paper samples were carried out using a nonlocal damage model on 2D rectangular samples with and without notches. The mesostructure of flocs and antiflocs was explicitly represented using a spatially correlated random field of the

Young's modulus distribution whose properties were experimentally obtained. The geometrical characteristics of the active FPZ (area and width) and their evolution during fracture were determined from damage field and were linked to the stress drop in the post-peak regime. A fracture test was carried out on a model paper with optical image recording. The FPZ was visually observed and characterized during the test. The comparison between the numerical and experimental results leads to a calibration of the internal length of the nonlocal damage model. The results are then compared to an explanatory analytical model. The article presents first the nonlocal stress-based model. The methodology to obtain the geometrical parameters of the FPZ from experiments and numerical simulation is secondly presented. The results are then presented to end with a final conclusive part.

2. Problem statement

This section aims at presenting the isotropic damage model which was used in this work to model the tensile fracture behaviour.

2.1. Nonlocal Mazars' damage model formulation

In an isotropic damage model, the progressive degradation of the material is represented by a damage scalar variable D [36]. Then, the constitutive law links the Cauchy stress tensor $\boldsymbol{\sigma}$ and the small strain tensor $\boldsymbol{\epsilon}$ by:

$$\sigma_{ij} = (1-D)\hat{\sigma}_{ij} = (1-D)C_{ijkl}\epsilon_{kl} \tag{1}$$

where σ_{ij} and ϵ_{kl} are respectively the components of the stress and strain tensor. C_{ijkl} corresponds to the components of the stiffness tensor and $\hat{\sigma}_{ij} = C_{ijkl}\epsilon_{kl}$ is the stress components of the effective non-damaged material. The value of the damage variable D varies during the loading from 0 (for a sound material) to 1 (for a fully damaged material).

The nonlocal damage criterion f_{nl} is determined from a nonlocal equivalent stain $\overline{\epsilon_{eq}}$ and an internal variable κ as:

$$f_{nl} = f\left(\overline{\epsilon_{eq}}, \kappa\right) = \overline{\epsilon_{eq}} - \kappa \tag{2}$$

The internal variable starts at a threshold level $\kappa = \epsilon_{d0}$ and is further updated as:

$$\kappa = \max_{t}\left(\overline{\epsilon_{eq}}\right) \tag{3}$$

where t is a pseudo-time variable. Therefore, $f_{nl} = 0$ during damage growth and $\dot{\kappa} = 0$ during unloading.

Giving that we interested in the modeling of paper failure in traction, we made the pragmatic choice to use the local equivalent strain ϵ_{eq} proposed by Mazars', based on the extension strains [37]. This value is calculated with the second invariant of the positive part of the strain tensor which represents the opening of microcracks yielding to the damage of the material:

$$\epsilon_{eq} = \sqrt{\langle\epsilon_{11}\rangle_+^2 + \langle\epsilon_{22}\rangle_+^2 + \langle\epsilon_{33}\rangle_+^2} \tag{4}$$

where ϵ_{ii} corresponds to the principal strains and $\langle x\rangle_+$ the positive part of x ($\langle x\rangle_+ = x$ if $x > 0$ and $\langle x\rangle_+ = 0$ otherwise).

The evolution law of the damage variable D in traction according to κ is [37]:

$$D(\kappa) = 1 - \frac{\epsilon_{d0}(1 - A_t)}{\kappa} - \frac{A_t}{e^{B_t(\kappa - \epsilon_{d0})}} \tag{5}$$

The Mazars' damage model, out of the elastic part, involves in traction a total of three parameters ϵ_{d0}, A_t, B_t to be identified on experimental tests. The parameter ϵ_{d0} corresponds to the nonlocal equivalent strain at the damage initiation. The parameter A_t controls the fraction of residual stress when damage tends towards unity and B_t manages the post-peak form of the tensile curve.

2.2. Integral nonlocal stress-based strain field

In this work, the nonlocal equivalent stain $\overline{\epsilon_{eq}}$ was determined using the stress-based nonlocal integral regularization proposed by Giry et al. [15].

In a nonlocal integral regularization, the nonlocal equivalent strain $\overline{\epsilon_{eq}}$ is obtained by averaging the local counterpart ϵ_{eq} by means of a weight function ϕ (convolution product):

$$\overline{\epsilon_{eq}}(x) = \int_{\Omega} \phi(\boldsymbol{x}, \boldsymbol{s}).\, \epsilon_{eq}(\boldsymbol{s}) d\boldsymbol{s} \tag{6}$$

The weight function describes the nonlocal weighting used in the averaging and is a function of the distance between the point $\boldsymbol{x}$ considered and each point $\boldsymbol{s}$ (called the distributing point) in the neighbourhood. The Gaussian form is used to describe the weighting. The weight function is also normalized to ensure the consistency of the relationship in the case of a uniform field:

$$\begin{cases} \phi_0(\boldsymbol{x}, \boldsymbol{s}) = \exp\left(-\left(\dfrac{4\|\boldsymbol{x} - \boldsymbol{s}\|^2}{l_c^2(\boldsymbol{x}, \boldsymbol{\sigma}(\boldsymbol{s}))}\right)\right) \\ \phi(\boldsymbol{x}, \boldsymbol{s}) = \dfrac{\phi_0(\boldsymbol{x}, \boldsymbol{s})}{\int_{\Omega} \phi_0(\boldsymbol{x}, \boldsymbol{s}) d\boldsymbol{s}} \end{cases} \tag{7}$$

with l_c the internal length. In the stress-based formulation, l_c corresponds to a characteristic length l_{c0}, assumed to be solely a function of the material structural scales, modulated by an influence factor ρ depending on the stress state $\boldsymbol{\sigma}(\boldsymbol{s})$:

$$l_c(\boldsymbol{x}, \boldsymbol{\sigma}(\boldsymbol{s})) = \rho(\boldsymbol{x}, \boldsymbol{\sigma}(\boldsymbol{s})) l_{c0} \tag{8}$$

The influence factor ρ is defined using spherical coordinates (ρ, θ and ϕ) in all directions in space by an ellipsoid centered at $\boldsymbol{s}$, with radius $\rho(\boldsymbol{x}, \boldsymbol{\sigma}(\boldsymbol{s}))$ in the $\boldsymbol{u} = \boldsymbol{x} - \boldsymbol{s}$ direction and oriented along the principal stress directions at point $\boldsymbol{s}$.

$$\rho(\boldsymbol{x}, \boldsymbol{\sigma}(\boldsymbol{s}))^2 = \frac{1}{f_t{}^2 \left(\dfrac{sin^2(\phi) cos^2(\theta)}{\sigma_1^2} + \dfrac{sin^2(\phi) sin^2(\theta)}{\sigma_2^2} + \dfrac{cos^2(\phi)}{\sigma_3^2}\right)} \tag{9}$$

σ_i is the principal stress in the direction i. The tensile limit stress f_t is considered so that the influence factor is equal to $\frac{|\sigma_i(s)|}{f_t}$ in the principal directions and the value of l_c is equal to l_{c0} at tensile peak for uniaxial loading. The interested reader can refer to [15] for more information on the performance of such an approach. At the end, the characteristic length l_{c0} still needs to be identified from the characteristic lengths of the material. In this contribution, we worked to advance in the direction of identifying l_{c0} as a function of the material structural scales.

3. Numerical and experimental methods to characterize crack propagation in paper

This section aims at presenting experiments and the stochastic finite element model of paper samples under tensile load, used to characterize in the third section the FPZ evolution.

3.1. Material

Two model papers were designed for the study. They were made of softwood flexible fibers of arithmetic mean fiber length $l_f = 1.35\ mm$ (mean length weighted-length $2.1\ mm$), measured using MOrFI® device (Techpap, Grenoble, France). The papers were manufactured using a Rapid-Köthen sheet former [28] which allowed elaborating “on demand” papers with more or less heterogeneous formations:

- The paper denoted HT (HeTerogeneous) corresponded to a paper that exhibited flocs and antiflocs.
- The one denoted HM (HoMogeneous) corresponded to a paper as homogeneous as possible with the Rapid-Köthen sheet former.

The measurements of the paper thickness and basis weight were determined using standard processes ISO 534:2011(F) and ISO 536:2019 respectively. The HT and HM papers had a standard thickness equal to $127\ \mu m$ and $113\ \mu m$ and a basis weight of $60\ g.m^{-2}$ and $50\ g.m^{-2}$, respectively. The main properties of the papers are summarized in Table 1.

Since the HT paper was arbitrary used as the reference paper for calibrating the mechanical model, we needed the local mechanical properties of the formation. Using tensile tests on a population of flocs and antiflocs, the HT paper was shown to exhibit a heterogeneous elastic modulus distribution at mesoscale which can be identified to a lognormale distribution of a mean value $1.5 \times 10^2\ kN/m$ and of a standard deviation $7 \times 10^1\ kN/m$. The results were taken from the experiments described in [28].

	Mean thickness (μm)	**Global basis weight ($g.m^{-2}$)**	**Mean fiber length (mm)**	**Formation**
HM	113	50	1.35	Homogeneous
HT	127	60	1.35	Heterogeneous

Tab. 1 Properties of paper material and associated samples

3.2. Macroscopic tensile test

Firstly, a unnotched sample type, denoted I, was cut in the HT paper sheet and had a height of $20\ mm$ and a width of $50\ mm$. We verified that the sample dimensions ensured a quasi-static fracture. Secondly, a notched sample type, denoted II, was cut on the HM paper and has a height of $50\ mm$ and a width of $25\ mm$. The notch of $3.5\ mm$ long was cut at the middle right of the sample. The notch length was chosen wide enough to initiate damage at notch tip while not taking it too wide to have a large enough crack path to do the analysis of the FPZ evolution. This sample was used as a validation experiment case for numerical results, as explained latter. Lastly, the length of the sample II was taken height enough to ensure that crack path did not interact with clamps. The geometry of samples is summarized in Figure 1-a.

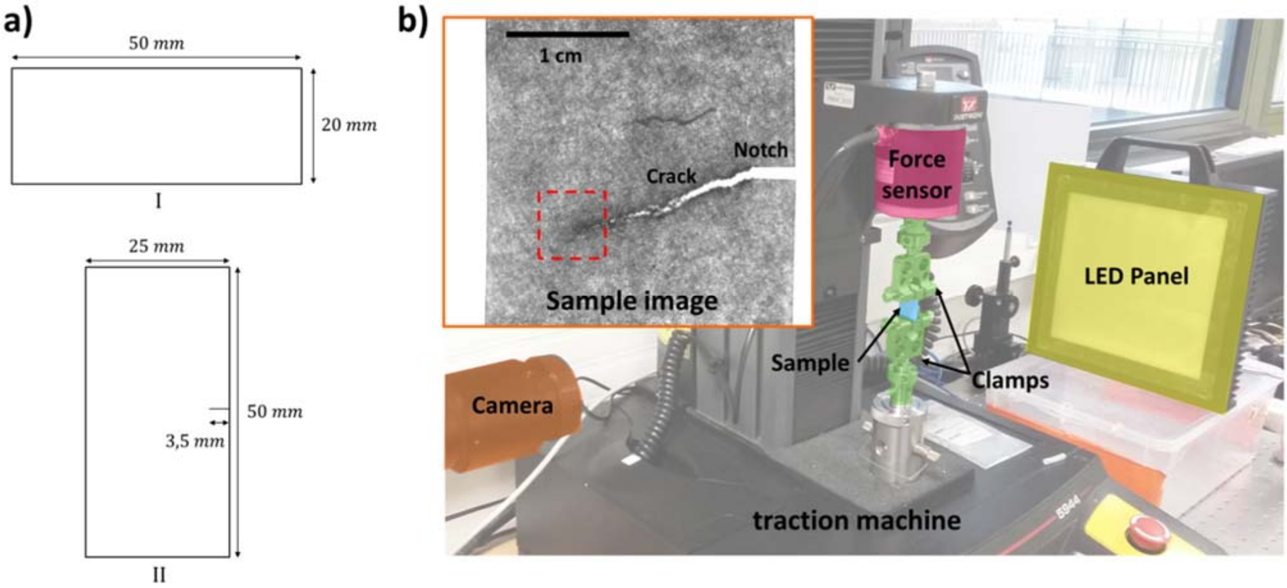

Fig. 1 **a** Sample geometry (I, II); **b** Experimental setup of a fracture test of a notched sample under uniaxial tensile loading. The sample is transmission lightened by a LED panel. Optical images of the sample are recorded during the test by a CCD camera. An example of image of the sample during fracture is shown in the box. The dotted red square indicates the crack tip neighbourhood

The displacement controlled tensile tests were carried out on both samples on the Instron® 5944 machine equipped with a $5\ kN$ force sensor at a strain rate of $0.2\ min^{-1}$. This strain rate was chosen as a compromise between low enough to neglect the inertial forces in the equilibrium of the system and high enough to minimize the creep due to the viscoelastic behaviour of the paper. In order to follow the evolution of the cracking during the tensile test, the sample II was illuminated by transmission with a $20 \times 20\ cm^2$ LED panel and filmed by a CCD camera (13 frames per second, the resolution corresponds to $0.01\ mm$ in the sample plane) during the tensile test (Figure 1-b). Data acquisition from the camera and the tensile machine were synchronized. The stress was obtained by dividing the force F acquired by the initial sample section $S_0 = w \times t$ with t and w the sample standard thickness and width, respectively.

3.3. Stochastic finite element modelling of samples under tensile load

As for the experiment part, two virtual samples were modelled in 2D with the finite element code CAST3M [38]. The first one was a unnotched sample of 20 mm height and of 50 mm wide as in the physical experiment (sample I). The second one was a notched sample of the same dimension that the previous one. The notch was placed in the middle right with a length of 15 mm and an arbitrary width of 1 mm. Trial and error simulations have shown that 15 mm allowed the notch to play a role in cracking (negligible influence of the boundary) while leaving a sufficient crack path to perform the analysis of the FPZ evolution. The notch length required for this purpose in the numerical model is much larger than the one in physical experiments. This may be due to either the modelling of the spatial variability of the Young's modulus in a continuous manner or the notch width with a lower singular effect in the numerical model at the tip. Although the experimental and the numerical notch lengths differ which may influence the crack initiation from the notch tip, they do not influence the FPZ propagation in its permanent regime which is the scope of our contribution.

The geometry of samples is illustrated in Figure 2. The dimensions of both virtual samples were chosen identical since the damage model parameters are identified on the unnotched sample and could be different due to the size effect of fracture process.

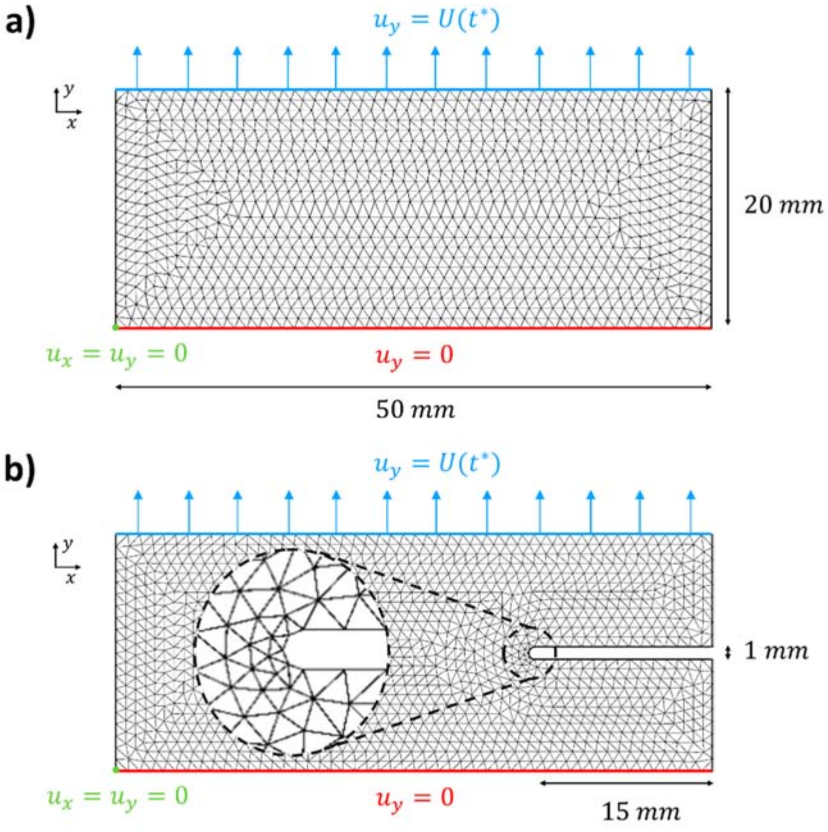

Fig. 2 Geometry, mesh and boundary conditions of: **a** the unnotched and; **b** the notched virtual samples. $\boldsymbol{u_x}$ and $\boldsymbol{u_y}$ are the horizontal and vertical displacement, respectively. $\boldsymbol{U}(\boldsymbol{t}^*)$ is the imposed displacement at the pseudo-time step $\boldsymbol{t}^*$.

Since the thickness of the paper is negligible regarding the in-plane dimensions, 2D stress plane conditions were assumed. The boundary conditions are described in Figure-2: the vertical displacement u_y is blocked along the bottom edge. The horizontal displacement u_x is additionally blocked on the bottom left point. The displacement $U(t^*)$ is imposed on the top edge linearly increasing according to the pseudo-time step t^*. The initial displacement step is specified at 2.5 10^{-5} m since it is small enough to have no influence on the results. In the strongly non-linear steps of the simulation, the code may automatically decrease this displacement step to facilitate the convergence. The mesh was made of linear triangular elements. The size of the elements is set equal to 1 mm with a refinement at the notch tip.

The paper behaviour was modelled by an elasto-damage constitutive model as introduced in section 2. The identification of the parameters A_t, B_t and ϵ_{d0} of the damage law against an experimental curve is detailed next.

In order to represent material mesostructure, a random field on the finite elements of the Young's modulus was set [39]. The field characteristics were based on the local Young's modulus distribution found for the HT paper [28].

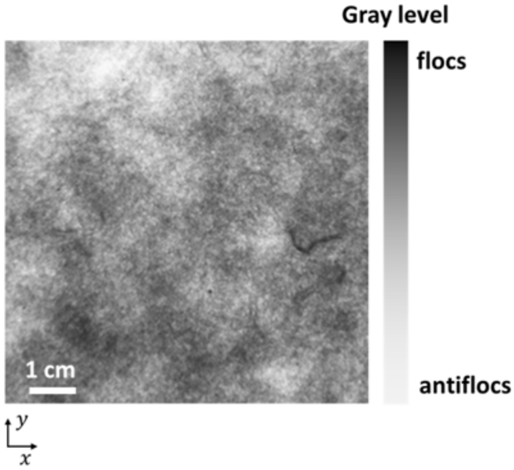

Fig. 3 Gray scale image of the paper in transmitted light

First, the random field E that represented the spatial variability of Young's modulus was identified. The random field is completely described by its mean μ_E, standard deviation σ_E, and autocorrelation function C_E (model with its associated autocorrelation length l_{corr}). Dividing the mean value and the standard deviation of elastic modulus (1.5×10^2 kN/m and 7×10^1 kN/m, respectively) of the HT paper by a constant thickness equals to the standard one of the HT paper ($= 127$ μm), the following mean value and standard deviation of Young's modulus were taken: $\mu_E = 1.2$ GPa and $\sigma_E = 0.6$ GPa. Besides, the authors showed that local elastic modulus increases with the local basis weight. Based on this observation and since the local basis weight variation can be visually observed by transmitted light as a local variability of opacity, the local Young's modulus spatial distribution was identified to the local basis weight variation using the gray scale of an image of the HT paper in transmitted light (Figure 3).

Methods characterizing the local basis weight distribution are based on optical image analysis of transmission lightened papers. The local basis weight distribution is mainly characterized by the local basis weight variation coefficient [25] or Fourier transform [40]. The use of variograms also makes it possible to characterize the basis weight distribution. Initially developed in the field of geostatistical [41], the variogram characterizes the spatial correlation of a variable, here the local basis weight *i.e.* gray levels. The interest of such an approach is that the variogram gives directly access to the autocorrelation function of the variable. In this work, the autocorrelation function C_E of the random field E and its autocorrelation length l_{corr} were identified from the variogram of the gray scale image of the HT paper in transmitted light, by the formation analyser Techpap® (Figure 3). The variogram allowed studying the spatial variability of the gray level of the paper. The variogram $\gamma(h)$ corresponds to the variance expected between two observation points (here pixels of the image) at a distance h from each other. For an isotropic stationary random field, the normalized variogram γ_{norm} is related to the autocorrelation function of the random field by:

$$\gamma_{norm}(h) = \frac{\gamma(h)}{\sigma_E} = \left(1 - C_E(h)\right) \tag{10}$$

For the sake of simplicity, the variogram along the principal directions of the image was considered to identify the autocorrelation function. Since the Rapid-Köthen sheet former generates isotropic papers as shown in [42] with two superimposed variograms in both directions, this choice seemed relevant. However, a portion of the tested samples was not enlighten uniformly along the y-axis, probably because of the lightening device. On the contrary, the lightening was completely uniform along the x-axis and ensured the stationarity of the variogram. Then, the x-axis was solely used to determine the variogram.

The normalized variogram along the x-axis of the gray scale image is represented in Figure 4-a. The experimental variogram showed that the spatial variability of grayscale can be well approximated by an exponential form (dotted line). Therefore, an exponential model was taken as the autocorrelation function with the corresponding autocorrelation length $l_{corr} = 7\ mm$.

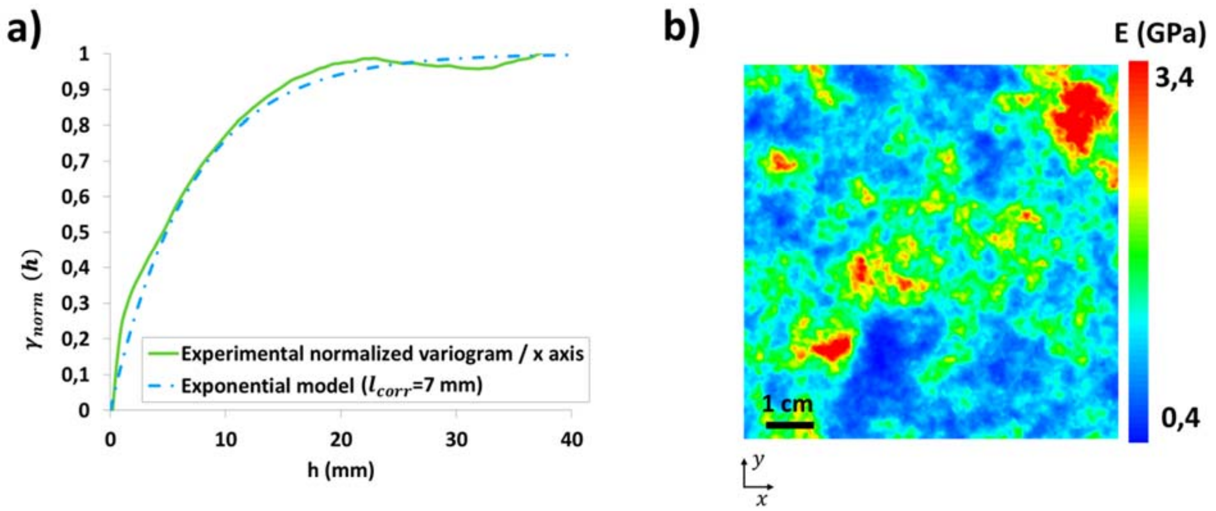

Fig. 4 **a** Corresponding experimental normalized variogram γ_{norm} according the x-axis (line) and the exponential model of the autocorrelation function with $l_{corr} = 7\ mm$ (dotted line); **b** A realization of the $10 \times 10\ cm^2$ area random field on Young's modulus

The identified theoretical random field was then projected onto the mesh using the rotating band method [43] available in CAST3M. Figure 4-b shows an example of a generated Young's modulus realization.

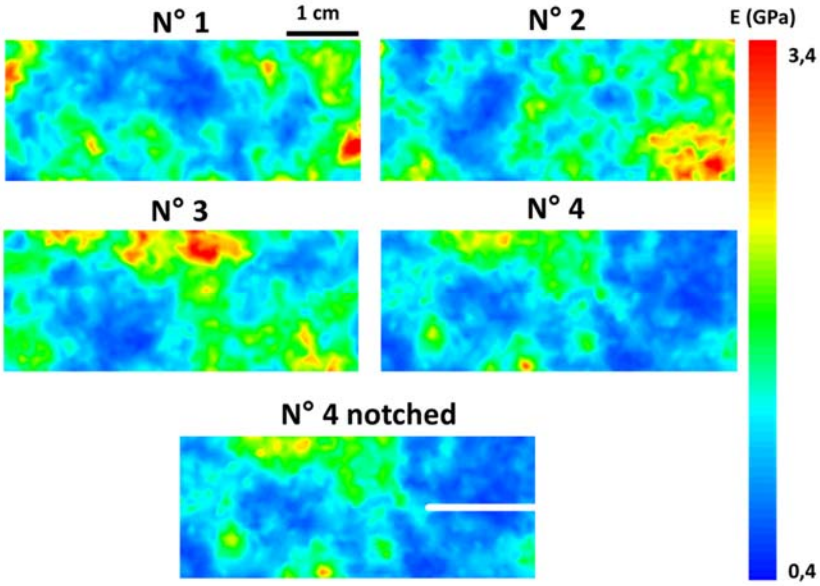

Fig. 5 The four realizations of the random field on Young's modulus used in this work (unnotched sample). The realization n°4 is also used for the notched sample

Four realizations of Young's modulus from the same random field were generated on unnotched sample type, denoted distribution n°1, 2, 3 and 4 on Figure 5. In a second part of this work, the crack propagation on a notched sample was studied on the fourth realization of Young's modulus, arbitrarily chosen.

The stress-based nonlocal Mazars' damage law was used here for the damage calculation with an internal length l_c arbitrarily taken to 6 mm. The influence of the internal length on the results is discussed at the end of the article.

The behaviour of the paper was modelled here in linear elastic damageable. However, the paper has non-linear elastic and plastic deformations. Unfortunately, to the best author knowledge, there is no elasto-plastic-damageable model accepted in the paper community. Therefore, the tensile curves from the simulations cannot be directly compared to an experimental curve if one wishes to neglect these nonlinear deformations in the model. For the sake of simplicity to split apart the different phenomena, the material was then modelled with an elasto-damage behaviour without introducing hardening and plasticity.

As fracture propagation (softening behaviour) is driven by the dissipation of the stored elastic into the FPZ, it seems relevant to estimate as accurate as possible the evolution of the stored elastic energy during tensile test. As plastic deformations dissipate energy before crack propagation, a part of the injected energy to the sample does not participate to fracture. Given that the hardening is not part of the model, the simplest way to not take into account the plastic energy from a tensile curve is to remove the plastic energy in the pre-peak assuming a linear elastic behaviour during discharge.

Figure 6-a shows a typical tensile curve for the paper used in this experiments. Assuming that: (i) all nonlinearities before the peak load were due to plastic deformations, (ii) a purely linear elastic discharge and (iii) only damage (i.e. no plasticity) occurred starting from the peak load, the total cracking energy w_f is represented by the area under the gray curve and the energy dissipated in plastic deformation w_{pl} is

represented by the white area under the curve. To calibrate an elasto-damageable model on such a curve means to take into account w_{pl} not as plastic energy dissipation but as cracking energy. Since an elasto-damageable model does not take plastic deformations into account, the tensile curves of the simulations are compared with the modified experimental curve from which the plastic deformations have been removed before the peak (Figure 6-b).

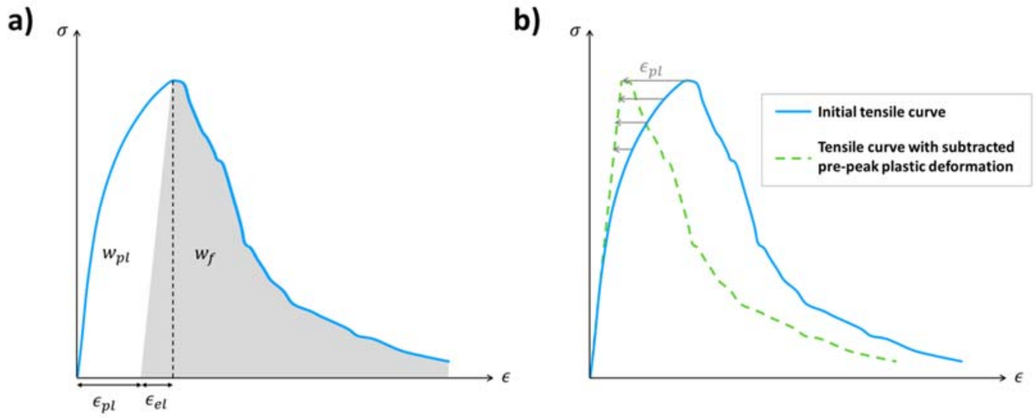

Fig. 6 a Experimental tensile curve of paper. The fracture energy $\boldsymbol{w_f}$ corresponds to the gray area. The energy dissipated into plastic deformations is the white area $\boldsymbol{w_{pl}}$. The contribution of the elastic and plastic deformation, respectively $\boldsymbol{\epsilon_{el}}$ and $\boldsymbol{\epsilon_{pl}}$, at peak load is represented; **b** Transformation of the initial tensile curve (—) subtracting the plastic deformations in the pre-peak (- -)

The parameters, A_t, B_t and ϵ_{d0} of the Mazars' damage law were identified by trials and errors from experimental tensile tests on three specimen of sample type I. The plastic deformations of the experimental curve were subtracted according to the method explained above. The parameter ϵ_{d0} is the strain at which damage begins. After several trials of values, we chose to take $\epsilon_{d0} = 0.01$. The coefficients A_t and B_t influence the shape of the post-pic. A_t defines the value of the asymptote of the curve for $\epsilon \rightarrow \infty$ (value of the residual stresses). In this case, there were no residual stresses because the specimen was fully cracked at the end of the test. This is equivalent of taking $A_t = 1$.

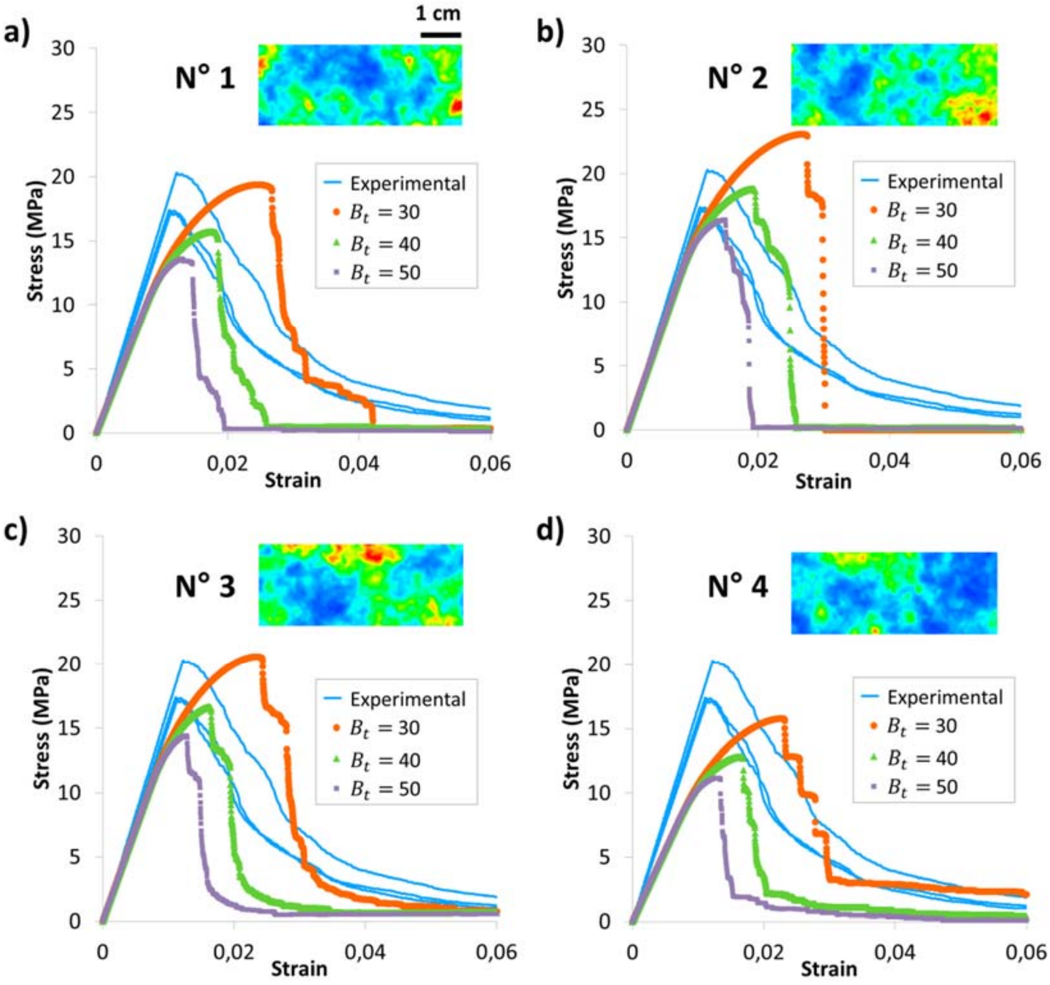

Fig. 7 Identification of $\boldsymbol{B_t}$ for the four realizations of Young's modulus on unnotched samples. The curves obtained for $\boldsymbol{B_t} = \mathbf{30}, \mathbf{40}$ and $\mathbf{50}$ are compared to three experimental curves without plastic deformations. The corresponding realizations are represented as a reminder at the top right of each graph

B_t was deduced by best fitting the modelled curve to the experimental one. Figure 7 shows the tensile curves for the four generated samples and for three different values of B_t $(= 30\,;\ 40$ and $50)$ in each case. It was observed that the curves followed closely the pre-peak part of the experimental curve. Besides, for all the simulated B_t values, the post peak was more brittle than that of the experimental curve. This could be due to the intrinsic fragility of the Mazars' damage model. Indeed, in the sake of simplicity (only two parameters are needed to describe the shape of the post-peak regime) an exponential function is used with a sharp descending branch upon damage initiation. A less brittle response may be obtained only at the cost of adding material parameters which complicates the fitting process. In spite of these differences, and of the expected variability of the response curves from one random field to another, the most suitable value of B_t was 40. A lower value of B_t would have generated too much damage before the peak and would have modified its value.

3.4. Experimental and numerical characterization of the FPZ evolution

As explained above, the process zone can be visually observed on paper samples. When the inter-fiber bonds break, new fiber surfaces are exposed to the transmitted light air. This alters the path, as the diffusion coefficient of the paper increases. Thus, if paper is transmission lightened, the area where the damage occurs becomes progressively darker. Starting from this observation, an original image analysis was developed to determine the evolution of the damage zone during an experimental tensile test from optical images. In order to compare the results with the numerical modelling, the same method was extended to numerical results considering in this case the damage field instead of optical image. All image analyses were performed using ImageJ software [44].

The method, illustrated in Figure 8 for both experimental and numerical results, was based on the point to point difference of images at two imposed strains ϵ and $\epsilon + \Delta\epsilon$, of the transmission-illuminated specimen (damage field for numerical samples) during the crack development. The strain increment $\Delta\epsilon$ was taken equal to 2×10^{-4} and 9×10^{-4} for experimental and numerical characterizations, respectively. In each case, the strain increments were sufficiently large so that the damage increase between the two instants was significant enough to be discernible on the image processing and sufficiently small to follow the evolution of the geometrical characteristics of the FPZ during the post peak.

Starting from two images at two imposed strains ϵ and $\epsilon + \Delta\epsilon$, denoted A and B respectively, the successive following steps were applied (see Figure 8 for illustration):

i. The point to point difference $B - A$ of the two images allowed to visualize an area where darkening occurs (blue) in front of the crack tip (red). Since the darkening zone corresponded to the damaged zone between the two states A and B, this zone was denoted “active FPZ”.
ii. In the experimental case, due to paper texture and strains outside the active FPZ, artifacts appeared on the image differences. Nevertheless, two successive images were considered to be taken at sufficiently close macroscopic deformations ($\Delta\epsilon = 2 \times 10^{-4}$ for experiments) and the contribution of these artifacts was localized, of size a_l, which allowed us to eliminate them by filtering (averaging filter of size a_l). Then, only the active FPZ was retained. As the damage field can be represented on the undeformed mesh during simulation, this step can be avoided in image analysis of numerical results.
iii. The final path of the crack was obtained from the image at the end of the test and considering the local direction of the crack. This path was superimposed on the current image. The local orientation of the crack at the crack tip was deduced.
iv. A thresholding was performed on the filtered image (ii). For experimental ones, the threshold was chosen to keep only the darken zones. For numerical ones, the threshold was arbitrarily chosen as zones where the increment of damage is such that $\Delta D > 0.05$.
v. The thresholded area was then approximated by an ellipse (on ImageJ using tool "Particles Analysis"). The ellipse found was then adjusted so that its major axis is oriented according to the local direction of the crack previously identified.
vi. The active FPZ was finally represented by an ellipse whose area and width can be calculated.

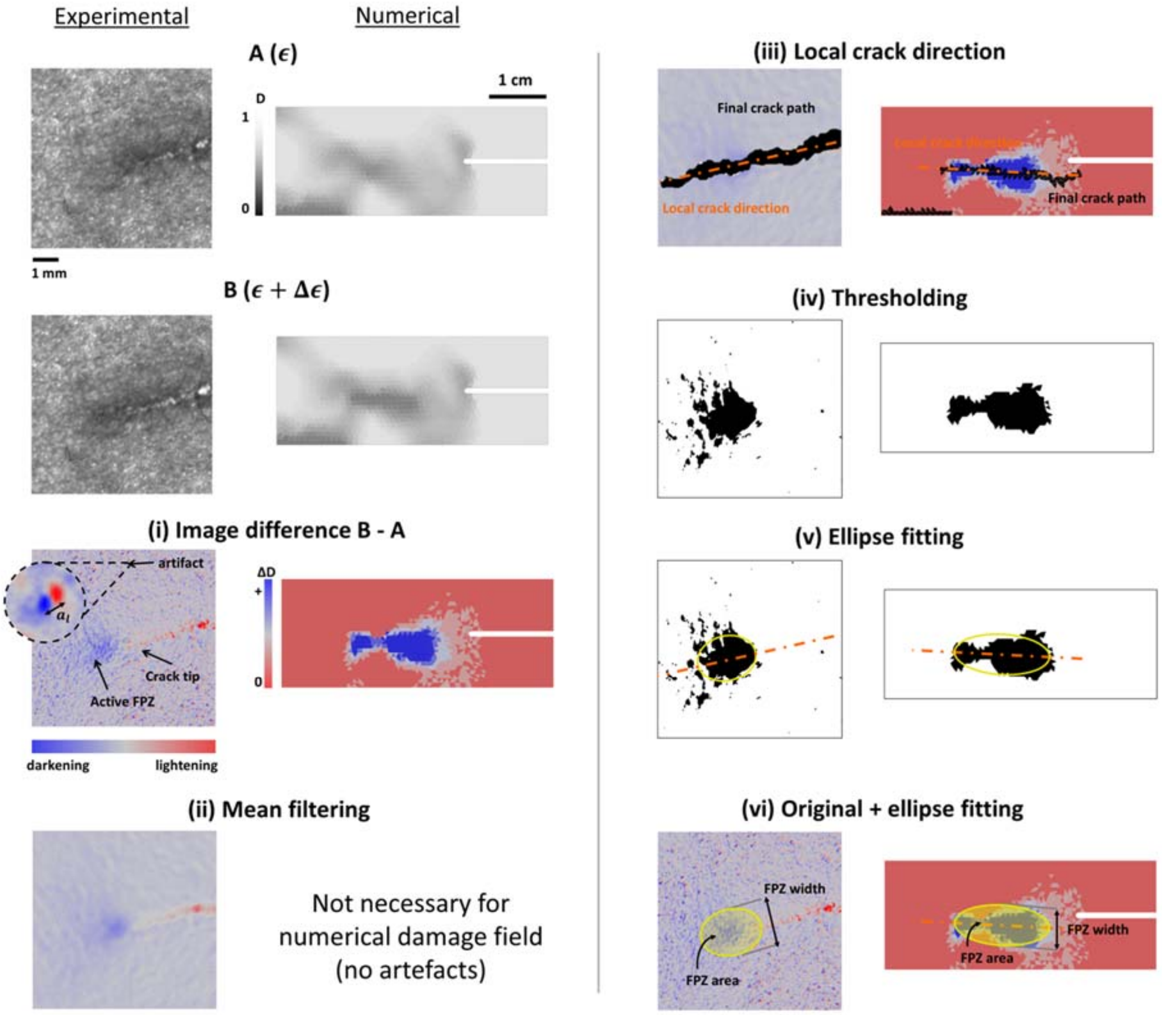

Fig. 8 Successive steps of the image analysis for the characterization of the active FPZ. For each step, left correspond to the experimental results and right to the numerical one. The experimental images A and B correspond to the red box zone in Figure 1-b

Considering this image analysis over all the crack propagation, we can derive the geometrical characteristics of the active FPZ and their evolution during the sample rupture.

4. Results and discussion

4.1. Damage development and final path on unnotched samples

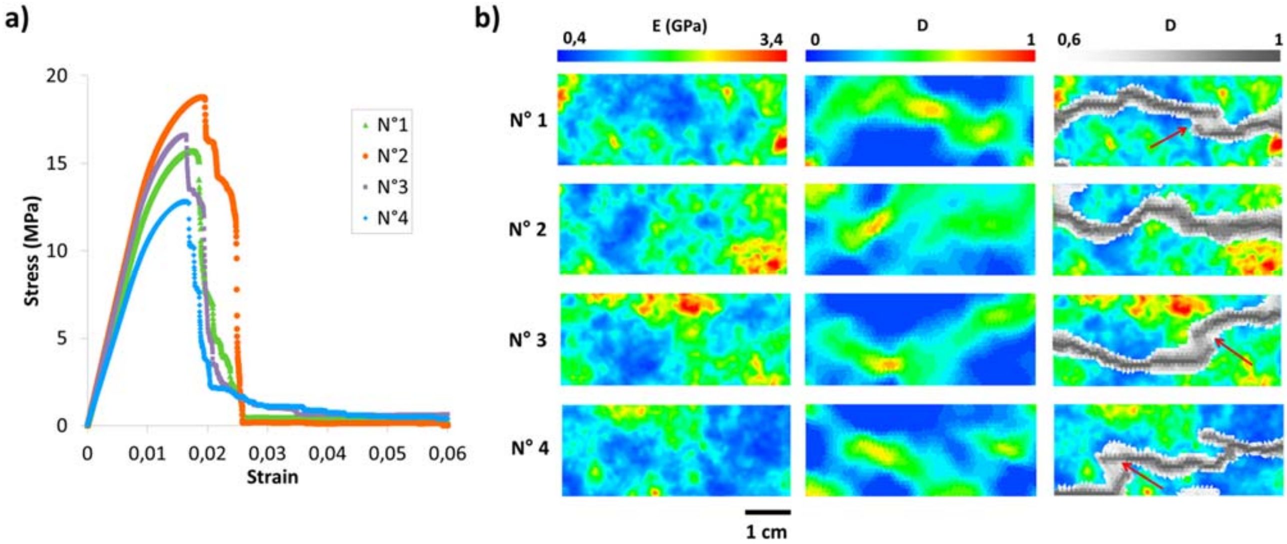

Fig. 9 Results of tensile tests on four unnotched samples with the four realizations of the random field of Young's modulus: **a** tensile curves; **b** (left) random field of Young's modulus. (middle) Corresponding damage field at the peak load. (right) Random field of Young's modulus with the damage field for $\mathbf{0.6 < D < 1}$ in gray scale at $\mathbf{6\%}$ of global deformation. The crack path corresponds to the zone where $\boldsymbol{D = 1}$. The red arrows show location where the branches are not still merged

Figure 9-a shows the tensile curves corresponding to the four Young's modulus realizations over the unnotched geometry. Although the four samples have been generated from the same random field, the response in particular the post-peak regime, varies significantly from a curve to another, probably due to the random presence of flocs and antiflocs and their relative position which may or may not create a continuous path with only antiflocs, for instance.

On Figure 9-b (middle column), the damage field at the peak force of each distribution is represented. It can be seen that the damage is concentrated in the low Young's modulus areas and across the entire width of the sample, giving that (i) with an homogeneous tensile test, local strains are larger in the low Young's modulus regions and (ii) the damage model is controlled in strain. The results are consistent with previous experimental observations on paper [45].

The right column of Figure 9-b shows the crack paths at 6% of global strain for the four Young's modulus field realizations. In each case, the crack avoids the high Young's modulus areas (flocs) to pass through the low Young's modulus areas (antiflocs) where the damage has initiated first. It should be noted that on sample n°4, the crack passes locally through the lower edge of the sample. This phenomenon could be avoided by taking higher samples so that weak points exist far from the edges. It is also interesting to see that on this same realization, the crack path admits several branches, which try to merge. It explains the non-fragility of the global response observed on the corresponding curve with a higher level of dissipated energy. The same remark can be made to a lesser extent for the realizations n°1 and n°3 which have two branches not yet merged (red arrows on Figure 9-b).

The analysis of the results on unnotched specimens allowed to identify the adequate parameters of the damage law as well as to highlight the similarities with previous experimental work on the damage initiation. In particular, at the peak, the damage is concentrated in the weak points across the width of the samples.

4.2. Damage evolution on a notched sample depending of the internal length

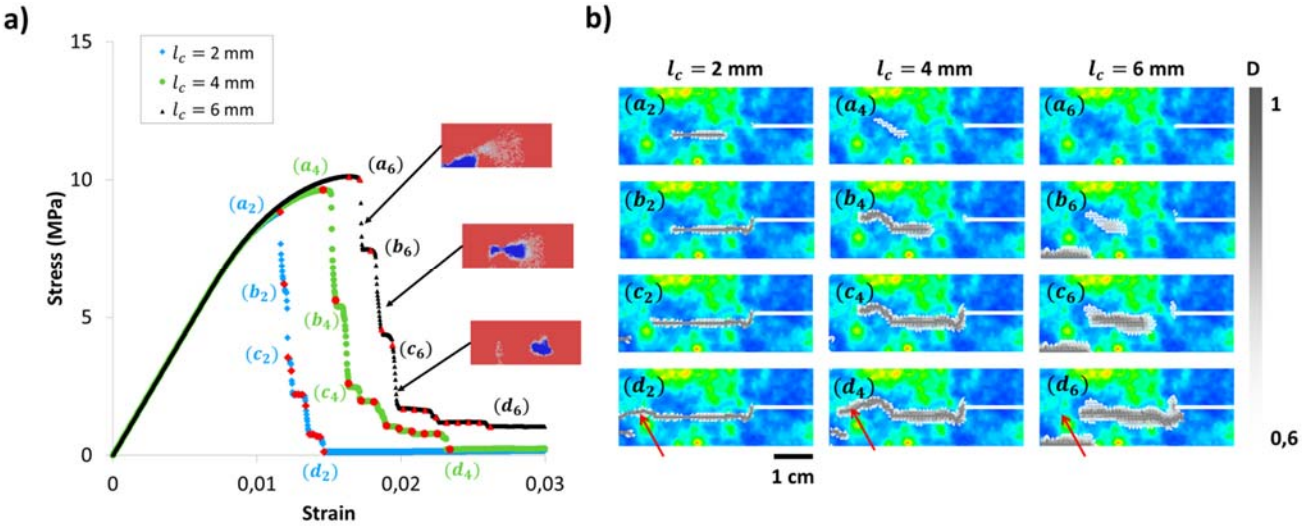

Fig. 10 Results of a tensile test on a notched sample with the realization n°4 of the random field of Young's modulus for three values of the internal length $\boldsymbol{l_c}$ (= $\mathbf{2}$; $\mathbf{4}$ and $\mathbf{6}\ \boldsymbol{mm}$): **a** tensile curves. The image analysis is performed considering only the damage field at the steps highlighted in red on the tensile curves. For $\boldsymbol{l_c = 6\ mm}$, the image difference of the damage field is shown at three steps for illustration in the boxes; **b** Young's modulus field with damage field ($\boldsymbol{0.6 < D < 1}$) for the steps (denoted $\boldsymbol{a}_{2,4,6}$; $\boldsymbol{b}_{2,4,6}$; $\boldsymbol{c}_{2,4,6}$ and $\boldsymbol{d}_{2,4,6}$ on tensile curves). Red arrows show the location where the final crack path depends on $\boldsymbol{l_c}$

Figure 10-a presents the tensile curves of the notched sample with the fourth Young's modulus realization for three values of l_c ($= 2$, 4 and 6 mm). On each curve, the red points correspond to the steps considered for the image analysis. The damage fields at the steps, denoted $ba_{2,4,6}$; $b_{2,4,6}$; $c_{2,4,6}$ and $d_{2,4,6}$ on the tensile curves, are represented in Figure 10-b.

For the different lengths simulated l_c, the damage initiation does not occur at the notch tip. Indeed, the location where the damage starts is the result of the competition between the notch tip stress concentration and the heterogeneity of the material which admits weak points where the damage tends to concentrate. It is worth reminding here that the mesh construction builds the notch tip with a circle, thus avoiding geometrical singularities. Besides, the Young's modulus realization admits a floc at the notch tip, making it stiffer. In this case, the damage starts in the antifloc ahead of the notch tip. Once the damage propagates into the weak points, the crack joins the notch tip and progressively propagates over the rest of the sample.

Differences in the crack path can also be noticed depending on the chosen internal length. For $l_c = 2\ mm$, the crack can pass through a narrow valley between 2 flocs. As l_c increases, the FPZ becomes wider and can no longer pass through a narrow valley (red arrows in Figure 10-b) because the large internal length will average out smaller deformations in the flocs. Therefore, a large internal length will favor passage through wide valleys.

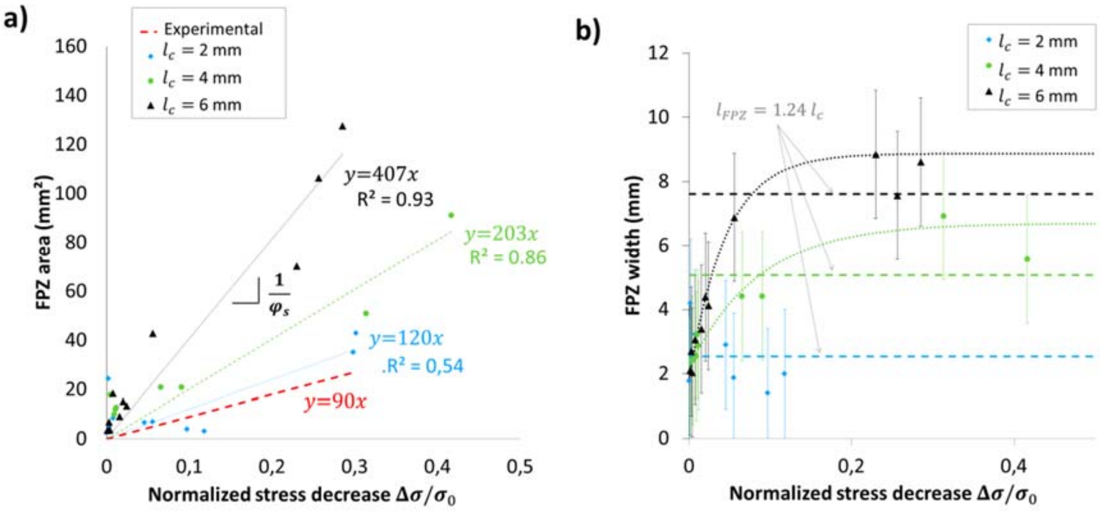

Fig. 11 a Area of the active FPZ according to the stress drop $\boldsymbol{\Delta\sigma/\sigma_0}$ between two steps spaced of $\boldsymbol{\Delta\epsilon}$ in the post peak regime (red ones in Figure 10-a). $\boldsymbol{\sigma_0}$ is the tensile strength. The dotted red line corresponds to the experimental results on the HM paper. The figure mentions the equation of the fitting and the correlation coefficient R²; **b** width of the active FPZ as a function of the stress drop $\boldsymbol{\Delta\sigma/\sigma_0}$ between two measuring points for different internal lengths. For $\boldsymbol{l_c = 4}$ and $\boldsymbol{6\ mm}$, the point distributions are approximated using an exponential law. Horizontal asymptotes represent the FPZ width $\boldsymbol{l_{FPZ} = 1.24\ l_c}$ predicted by the analytical model as discussed in the section 4.4

Considering the steps spaced of $\Delta\epsilon$ in the post peak regime (red points in Figure 10-a), (i) the tensile curve gives the stress drop between two successive steps and (ii) the image analysis presented above provides the geometrical characteristics (area and width) of the active FPZ between these successive steps. Figure 11 plots the active FPZ area and the active FPZ width giving the global stress drop $\Delta\sigma$ normalized by the tensile strength σ_0, for each l_c simulated. In Figure 11-a, the following observations can be made:

- The greater the normalized stress drop $\Delta\sigma/\sigma_0$, the larger the active FPZ area.
- For $l_c = 4$ and $6\ mm$, the stress drop may be fitted linearly with the active FPZ area ($R^2 = 0.86$ and 0.93, respectively). For $l_c = 2\ mm$, the variation of FPZ area is too small to conclude on the proportional relation, probably due to the mesh size not enough refined in this case since in average one has only 2 elements for the characteristic length.
- The slope increases with the internal length.

Although the linear relation between the local stress state and the interaction length is prescribed in Eq (9), it is worth checking that an identical relation may be highlighted between the global force and the FPZ size in order to simplify the fitting process in the future for non-local parameter. Indeed, due to (i) spatial variability, (ii) non linearities, (iii) strain localisation among others, this result was not obvious beforehand.

Assuming no plastic energy dissipation and considering ϵ constant in a stress drop, the volumetric energy $\Delta\Sigma$ which is released during a stress drop is $\Delta\Sigma = \frac{1}{2} \times \epsilon \times \Delta\sigma$. The global stress drop $\Delta\sigma/\sigma_0$ can thus be considered as an indirect measure of the energy released within the active FPZ. In this case, ϵ varies significantly in the post peak. However, as (i) the slope of proportionality between FPZ area and stress drop is mainly determined by high stress drop, (ii) the highest stress drops are the first ones and (iii) ϵ does not vary significantly in the first stress drops, we assume $\Delta\Sigma \propto \Delta\sigma$ with the same proportionality factor over the post-peak.

Thus, during damage process, the amount of energy released in the active FPZ grows with the volume of the active FPZ. The in-plane surface energy released in the active FPZ is defined as $\varphi_s = \varphi_v / t$ where φ_v is the amount of volume energy released and t the sample thickness equal to $127\ \mu m$, and is inversely proportional to the slope of each curve fitting in Figure 11-a. Judging the associated correlation coefficients, the linear fitting between the stress drop and the FPZ area is a relevant choice and therefore, we consider that φ_s remains constant in all the post-peak. Moreover, the slope $1/\varphi_s$ increases with the internal length: the crack propagates in the direction that requires the least amount of released energy. The larger the internal length l_c, the larger the FPZ width, the larger the volume where the energy is dissipated and therefore the smaller the volume released energy φ_v (then, the surface energy φ_s). The surface energy φ_s (l_c) is therefore a direct function of the internal length of the model.

Figure 11-b shows the influence of the internal length on the width of the active FPZ. Error bars corresponding to twice the mesh size (i.e. $2\ mm$) are added to the measurement points to represent the possible measurement error due to the mesh discretization. For $l_c = 4$ and $6\ mm$, the width of the FPZ increases with the stress drop until a limit value l_{FPZ}. For $l_c = 2\ mm$, the size of the measurement error is too large to distinguish an evolution of the FPZ width

4.3. Evolution of the FPZ size in paper during experimental fracture test

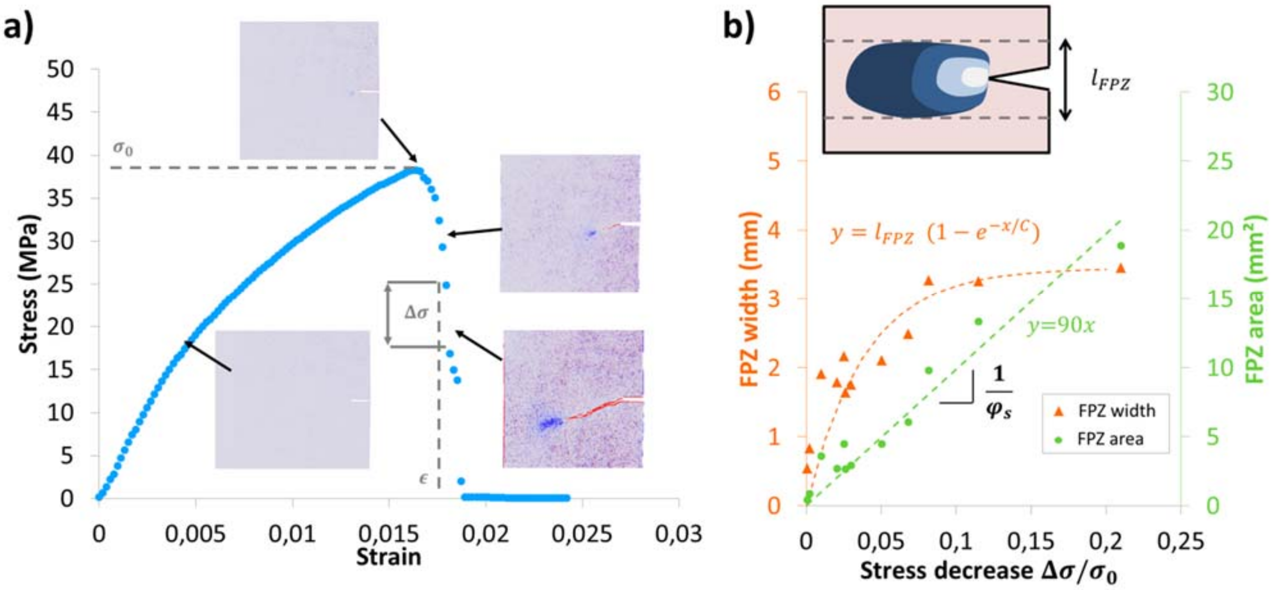

Fig. 12 a Tensile curve. The image differences allowing to see the evolution of the active FPZ are displayed at different moments of the test; **b** dimensions of the FPZ (area and width) as a function of the normalized stress drop $\boldsymbol{\Delta\sigma/\sigma_0}$ between two successive acquisition points on the tensile curve, where $\boldsymbol{\sigma_0}$ is the tensile strength. The area is proportional to the stress drop with a coefficient $\boldsymbol{1/\varphi_s\ = 90\ mm^2}$. The width evolution law is exponential and bounded by its limit value $\boldsymbol{l_{FPZ}}$. The insert shows the typical profile of the FPZ for different stress drops

In order to validate the behaviour observed in the numerical simulation, the same procedure of result treatment is applied to an experimental tensile test of fracture on a paper sample.

Figure 12-a shows the tensile curve for sample denoted II. For each measurement point along the curve, an image of the sample is recorded by the camera. Differences between images are presented, allowing the tracking of the development of the active FPZ during the tensile test. It is observed that the active FPZ appears from the stress peak and its dimensions change erratically during the post peak. Figure 12-b shows the changes in the width and area of the active FPZ as a function of the stress drop $\Delta\sigma$ normalized by the tensile strength σ_0. The mean size a_l of the artifacts was measured equal to $0.15\ mm$.

Like in the numerical results, the active FPZ area is proportional to the normalized stress drop. Giving the previous remark, it means that the amount of released energy during a stress drop is proportional to the active FPZ area. Then, the damage occurs with a constant surface energy released. This is not surprising giving that in paper, the damage is mainly due to the breaking of inter-fibers bond [3]. As the tested paper has a homogeneous formation, the degree of bonding is also expected to be homogeneous. Thus, as the released energy is the sum of the released energy from each fiber-fiber bond breakage, the surface energy released during the crack propagation is constant. For the tested sample, the coefficient $\frac{1}{\varphi_s}$ is equal to $90\ mm^2$, i.e. $\varphi_s = 1.1 \times 10^{-2}\ mm^{-2}$.

It is also observed that the width of the active FPZ varies with the stress drop up to a plateau. At first glance, this observation is not consistent with nonlinear damage theories which consider that the width of the FPZ remains constant. However, in our case, it should be remembered that the FPZ propagates in a heterogeneous fiber medium. In this case, a regime of establishing the damage zone in width is highlighted, which suggests that the aspect ratio of the damage zone changes during the crack propagation. The different profiles of the active FPZ are shown schematically in the insert of Figure 12-b. The active FPZ develops in width and length with the stress drop. A description of the development of the FPZ during the damage is proposed here: if the area of the active FPZ increases proportionally with the stress drop, its width gradually increases and stabilizes to reach a limit width l_{FPZ}. In Figure 12-b, the evolution of this width is illustrated: it can be approximated using an empirical exponential law and shows that the width of the FPZ increases up to a threshold value. Note that the artifacts size a_l is small enough to consider that the active FPZ dimensions are not affected by the elastic deformations of the sample.

Thus, the evolution of the damage zone can be summarized as follows: the crack propagates intermittently depending on fibers. The intermittent propagation of a crack in paper is known and highlighted using acoustic emission [46]. In a first regime, from the initiation of a crack propagation where the width of the active FPZ is zero and the stress drop is small, the FPZ grows progressively, both in width and length. Then, in a second regime, when the FPZ has reached its limiting width, it continues to grow only in length, in order to satisfy the conservation of the surface released energy φ_s. Damage in the crack direction progresses faster in the second regime.

4.4. Discussion by means of an analytical model

The limiting value l_{FPZ} of the FPZ width can moreover be found via an explanatory analytical model based on damage theory in continuous homogeneous media. Let consider a homogeneous solid of thickness t with a cracked zone of width l_{FPZ}. The solid is under a tensile force F (Figure 13-a), such that the cracked zone propagates over a length Δl. The change in resistant section ΔS is written:

$$\Delta S = t \times \Delta l \tag{11}$$

The variation of the force to which the solid is subjected during the propagation of the crack is written:

$$\Delta F = \sigma_0 \times \Delta S \tag{12}$$

where σ_0 is the material strength.

From equations (11) and (12), and based on the stress $\sigma = F/S_0$, the stress increment $\Delta\sigma$ is derived:

$$\Delta\sigma = \frac{\Delta F}{S_0} = \sigma_0 \times \frac{\Delta S}{S_0} = \sigma_0 \times t \times \frac{\Delta l}{S_0} \tag{13}$$

where S_0 is the initial sample section.

Denoting $l_0 = \frac{S_0}{t}$, the initial sample width, we deduce:

$$\frac{\Delta\sigma}{\sigma_0} = t \times \frac{\Delta l}{S_0} = \frac{\Delta l}{l_0} \tag{14}$$

Assuming that the material is homogeneous and the crack propagates in steady state, the active FPZ area a_{FPZ} is measured in the sample plan:

$$a_{FPZ} = \Delta l \times l_{FPZ} \tag{15}$$

Then:

$$a_{FPZ} = l_{FPZ} \times l_0 \times \frac{\Delta\sigma}{\sigma_0} \tag{16}$$

The area of the active FPZ and the stress drop are thus related by a linear dependence of slope: $\frac{1}{\varphi_s} = l_{FPZ} \times l_0$. The Figure 13-b plots the coefficient $\frac{1}{\varphi_s}$ from results in Figure 11-a according to the internal length l_c. The point (0, 0) is added by making the assumption that for an internal length equals to zero, the area of the active FPZ is zero (which is not exactly true in the finite element model due to the finite space discretization) for any stress drop (*i.e.* $\frac{1}{\varphi_s} = 0$). $\frac{1}{\varphi_s}$ is found to be proportional to l_c:

$$\frac{1}{\varphi_s} = k \times l_c \tag{17}$$

Giving that the initial sample width $l_0 = 50\,mm$, and $k = 62\,mm$ (Figure 13-b), it can be simply deduced:

$$l_{FPZ} = k \times \frac{l_c}{l_0} = 1{,}24 \times l_c \tag{18}$$

In Figure 11-b are added the values predicted by this model. These values are consistent with the asymptotes of the exponential laws. When looking the path of the FPZ, it runs almost entirely in the antiflocs (Figure 10-b). In other words, from the crack's point of view, the damage occurs in a relatively homogeneous medium consisting of all the weak spots in the sample.

The role of heterogeneities can therefore be summarized as follows. They influence the crack path, making it passing through a series of weak zones (antiflocs in paper) and bypassing the strong zones (flocs). With our original model, it can be deduced that the FPZ width is due to the microstructural characteristic size (as fiber length) in the weak zones (antiflocs) as long as the characteristic distance between two strong zones is large enough. However, the crack path orientation (roughness) and thus the final length both depend on the characteristic size of the strong zones which is rather the mean distance between flocs than their mean size.

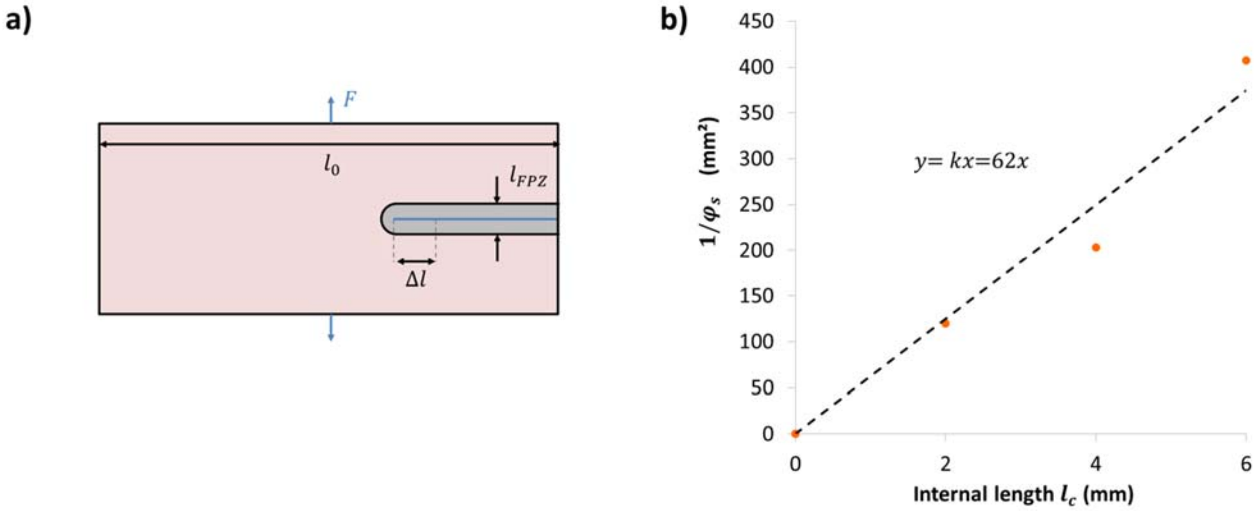

Fig. 13 **a** Representation of a crack progress on a length $\boldsymbol{\Delta l}$ with a FPZ width $\boldsymbol{l_{FPZ}}$ during tensile load; **b** coefficient $\boldsymbol{1/\varphi_s}$ vs. internal length $\boldsymbol{l_c}$ from the finite element model

4.5. Towards a new approach to identify the internal length

The direct observations in the HM paper allowed determining the surface energy φ_s in the FPZ during fracture. From the numerical and theorical analysis done in previous sections, it appeared that for the HT paper, the FPZ is located in the weak points (antiflocs) of the sample and its width is only due to the microstructural characteristic sizes and not to the mesostructure of flocs, too far from each other to interact in the FPZ. Then, as long as the HM and HT papers are constituted of the same fibers, we consider that the surface energy experimentally found can be used to fit the internal length in the damage model.

In Figure 11-a, the slope found experimentally on the sample II is added to the curves. It appears that an internal length l_c below $2\,mm$ must be taken to have the same slope, i.e. same φ_s. This result is consistent with the internal length found to be most suitable by Isaksson [33] in a finite element simulation of Kraft paper and printing paper (i.e., an internal length $l_c = 2 \times l_f$ with l_f the average fiber length). However, this result was obtained with a single fiber length. In this study, we observe that $l_c = 1.5 \times l_f$ which corresponds to the same range. Note in this work, the characteristic mesoscale sizes are explicitly represented by the random field. Then, the nonlocal nature of the damage is here due to the characteristic sizes at microscale (fibers). The difference between both results could be affected by the intrinsic brittleness of the local damage model. For instance, with the Mazars' model, an increase of the B_t coefficient can be compensated by an increase of the internal length to keep the same dissipated failure energy. Note that the parameters of the damage law were identified for $l_c = 6\,mm$. It would therefore be necessary to identify these parameters again for each internal length tested. However, in view of the differences observed between the experimental curves and the model, the calibration of B_t seems crude and it was not considered useful to recalculate it for the other internal lengths tested.

5. Summary and concluding remarks

In this work, the evolution of the FPZ during fracture of paper was investigated using a nonlocal damage model on a high density paper sample under tensile load. In order to represent the heterogeneities of paper at mesoscale, the Young's modulus was modelled using a random field. First, tensile tests on unnotched sample allowed calibrating the damage law parameters as well as the study of the influence of the random field on the damage development. The crack path was found to avoid flocs and thus FPZ remained in a relatively homogeneous medium consisting of antiflocs. The flocs only played the role of changing the crack path orientation and at the end of the developed crack length. Thus, the characteristic distance between flocs had an influence on the global fracture energy.

In a second part, the geometrical characteristics of the FPZ and their evolution during crack propagation were studied. From experimental observations, an original image analysis based on the successive images differences of the transmitted light sample acquired during tensile test was proposed. The image processing led to the characterization of the area and the width of an "active FPZ", i.e. the zone where the damage occurred between two considered steps. The image analysis was adapted for numerical modelling considering the local damage field in this case. It was found that:

- The area of the active FPZ a_{FPZ} and the normalized stress drop $\Delta\sigma/\sigma_0$ were related by a surface energy φ_s dissipated in the active FPZ: $a_{FPZ} \times \varphi_s = \Delta\sigma/\sigma_0$.
- The width of the active FPZ increased with the stress drop until it reached a limit value l_{FPZ} corresponding to a fully developed FPZ. Then, inside the weak zones, the width of the FPZ can evolve according to the characteristics of the heterogeneities at microscale (fibers) encountered. The FPZ can therefore stop from time to time, producing stress drops and width variations and the active FPZ can take two possible forms, probably depending on the flocs and antiflocs positions surrounding the FPZ: a circular one and a more slender one in the direction of the crack.

These results were also observed on an experimental tensile test of paper, which showed the good consistency of the nonlocal stress-based damage model to represent the post-peak behaviour.

Under the hypothesis of not accounting for the plastic energy, it was shown that the surface energy φ_s was a function of the internal length l_c of the nonlocal model. Thus, an internal length could be identified that was considered adequate when the value of $\varphi_s(l_c)$ matches the value found experimentally.

All of these results require to be confirmed by other random field realizations, in future research. We note that some samples in numerical simulation had part of the cracking path on their edges because the sample size was not large enough, although bi-traction was avoided in boundary conditions. We used a damage model based on an extension criterion. This choice was relevant since we modelled the paper failure in traction. Then, this choice may be questioned if the failure mode is not known beforehand.

In this work, the chosen random field allowed the development of the FPZ only in the antiflocs, that lead to conclude that, in this case, the mesostructure affected the crack path but not the FPZ development. The next question concerns the development of the damage zone when it cannot avoid the mesostructure elements of the material. If the issue was investigated using heuristic model [47], it would be interesting to study experimentally the behaviour of the FPZ, in particular its geometrical characteristics, when it interacts with the flocs.

6. References

1. Bažant, Z.P., Vořechovský, M., Novák, D.: Asymptotic Prediction of Energetic-Statistical Size Effect from Deterministic Finite-Element Solutions. J. Eng. Mech. 133, 153–162 (2007). https://doi.org/10.1061/(ASCE)0733-9399(2007)133:2(153)

2. Manouchehrian, A., Cai, M.: Influence of material heterogeneity on failure intensity in unstable rock failure. Comput. Geotech. 71, 237–246 (2016). https://doi.org/10.1016/j.compgeo.2015.10.004

3. Gustafsson, P.-J., Niskanen, K.: Paper as an engineering material. In: Niskanen, K. (ed.) Mechanics of paper products. pp. 5–26 (2012)

4. Fakoor, M., Shokrollahi, M.S.: A new approach for investigation of mode II fracture toughness in orthotropic materials. Acta Mech. 229, 3537–3556 (2018). https://doi.org/10.1590/1679-78253979

5. Bažant, Z.P.: Nonlocal damage theory based on micromechanics of crack interactions. J. Eng. Mech. 120, 593–617 (1994)

6. Hillerborg, A., Modéer, M., Petersson, P.: Analysis of crack formation and crack growth in concrete by means of fracture mechanics and finite elements. Cem. Concr. Res. 6, 773–782 (1976). https://doi.org/10.1016/0008-8846(76)90007-7

7. Wells, G.N., Sluys, L.J.: A new method for modelling cohesive cracks using finite elements. Int. J. Numer. Methods Eng. 50, 2667–2682 (2001). https://doi.org/10.1002/nme.143

8. Mühlhaus, H.-B., Aifantis, E.C.: A variational principle for gradient plasticity. Int. J. Solids Struct. 28, 845–857 (1991). https://doi.org/10.1016/0020-7683(91)90004-Y

9. De Borst, R., Mühlhaus, H.-B.: Gradient-dependent plasticity: Formulation and algorithmic aspects. Int. J. Numer. Methods Eng. 35, 521–539 (1992)

10. Pijaudier-Cabot, G., Bažant, Z.P.: Non local Damage Theory. J. Eng. Mech. 113, 1512–1533 (1987). https://doi.org/http://dx.doi.org/10.1061/(ASCE)0733-9399(1987)113:10(1512)

11. Geers, M.G.D., Peerlings, R.H.J., Brekelmans, W.A.M.: Phenomenological nonlocal approaches based on implicit gradient-enhanced damage. Acta Mech. 144, 1–15 (2000)

12. Pijaudier-Cabot, G., Haidar, K., Dubé, J.: Nonlocal Damage Model with Evolving Internal Length. Int. J. Numer. Anal. Methods Geomech. Wiley, 2004, Comput. Mech. Concr. Concr. Struct. 28, 633–652 (2004)

13. Krayani, A., Pijaudier-Cabot, G., Dufour, F.: Boundary effect on weight function in nonlocal damage

model. Eng. Fract. Mech. 76, 2217–2231 (2009). https://doi.org/10.1016/j.engfracmech.2009.07.007

14. Pijaudier-Cabot, G., Dufour, F.: Nonlocal damage model Boundary and evolving boundary effects. Eur. J. Environ. Civ. Eng. 14, 729–749 (2010)

15. Giry, C., Dufour, F., Mazars, J.: Stress-based nonlocal damage model. Int. J. Solids Struct. 48, 3431–3443 (2011). https://doi.org/10.1016/j.ijsolstr.2011.08.012

16. Eringen, A.C., Speziale, C.G., Kim, B.S.: Crack-tip problem in non-local elasticity. J. Mech. Phys. Solids. 25, 339–355 (1977). https://doi.org/10.1016/0022-5096(77)90002-3

17. Simone, A., Askes, H., Sluys, L.J.: Incorrect initiation and propagation of failure in non-local and gradient-enhanced media. Int. J. Solids Struct. 41, 351–363 (2004). https://doi.org/10.1016/j.ijsolstr.2003.09.020

18. Bažant, Z.P., Pijaudier-Cabot, G.: Measurement of characteristic length of nonlocal continuum. J. Eng. Mech. 115, 755–767 (1989)

19. Landis, E.N.: Micro-macro fracture relationships and acoustic emissions in concrete. Constr. Build. Mater. 13, 65–72 (1999). https://doi.org/10.1016/S0950-0618(99)00009-4

20. Grégoire, D., Verdon, L., Lefort, V., Grassl, P., Saliba, J., Regoin, J.-P., Loukili, A., Pijaudier-Cabot, G.: Mesoscale analysis of failure in quasi-brittle materials: comparison between lattice model and acoustic emission data. Int. J. Numer. Anal. Methods Geomech. 39, 1639–1664 (2015). https://doi.org/10.1016/j.solener.2019.02.027

21. Alam, S.Y., Saliba, J., Loukili, A.: Fracture examination in concrete through combined digital image correlation and acoustic emission techniques. Constr. Build. Mater. 69, 232–242 (2014). https://doi.org/10.1016/j.conbuildmat.2014.07.044

22. Zietlow, W.K., Labuz, J.F.: Measurement of the intrinsic process zone in rock using acoustic emission. Int. J. Rock Mech. Min. Sci. 35, 291–299 (1998). https://doi.org/10.1016/S0148-9062(97)00323-9

23. Le Bellégo, C., Dubé, J., Pijaudier-cabot, G., Gérard, B.: Calibration of nonlocal damage model from size effect tests. Eur. J. Mech. 22, 33–46 (2003)

24. Du Plessis, A., Boshoff, W.P.: A review of X-ray computed tomography of concrete and asphalt construction materials. Constr. Build. Mater. 199, 637–651 (2019). https://doi.org/10.1016/j.conbuildmat.2018.12.049

25. Sampson, W.W.: The structural characterization of fibre networks in papermaking processes - A review. Fundam. Res. Symp. 11th, 1205–1288 (2001)

26. Wong, L., Kortschot, M.T., Dodson, C.T.J.: Effect of formation on local strain fields and fracture of paper. J. Pulp Pap. Sci. 22, 213–219 (1996)

27. Alzweighi, M., Mansour, R., Lahti, J., Hirn, U., Kulachenko, A.: The influence of structural variations on the constitutive response and strain variations in thin fibrous materials. Acta Mater. 203, 116–460 (2021). https://doi.org/10.1016/j.actamat.2020.11.003

28. Villette, F., Rolland du Roscoat, S., Dufour, F., Bloch, J.-F., Baroth, J., Carré, B.: Toward the link between structural and mechanical properties of fiber aggregates in paper materials. J. Mater. Sci. 57, 7587–7599 (2022). https://doi.org/10.1007/s10853-022-07098-8

29. Kettunen, H., Niskanen, K.: Microscopic damage in paper. Part I: Method of Analysis. TAPPI. 83, 1–8 (2000)

30. Niskanen, K., Kettunen, H., Yu, Y.: Damage width: a measure of the size of fracture process zone. Sci. Papermak. 12th Fundam. Res. Symp. 2, 1467–1482 (2001)

31. Isaksson, P., Hagglund, R.: Acoustic emission assisted fracture zone analysis of cellulose fibre materials. J. Compos. Mater. 47, 2865–2874 (2012). https://doi.org/10.1177/0021998312459781

32. Isaksson, P., Dumont, P.J.J., Rolland du Roscoat, S.: Crack growth in planar elastic fiber materials. Int. J. Solids Struct. 49, 1900–1907 (2012). https://doi.org/10.1016/j.ijsolstr.2012.03.037

33. Isaksson, P., Hägglund, R., Gradin, P.: Continuum damage mechanics applied to paper. Int. J. Solids Struct. 41, 4731–4755 (2004). https://doi.org/10.1016/j.ijsolstr.2004.02.043

34. Isaksson, P., Hägglund, R.: Structural effects on deformation and fracture of random fiber networks and consequences on continuum models. Int. J. Solids Struct. 46, 2320–2329 (2009). https://doi.org/10.1016/j.ijsolstr.2009.01.027

35. Krasnoshlyk, V., Rolland du Roscoat, S., Dumont, P.J.J., Isaksson, P.: Influence of the local mass density variation on the fracture behavior of fiber network materials. Int. J. Solids Struct. 138, 236–244 (2018). https://doi.org/10.1016/j.ijsolstr.2018.01.016

36. Lemaitre, J.: Evaluation of dissipation and damage in metals submitted to dynamic loading. (1971)

37. Mazars, J.: A description of micro- and macroscale damage of concrete structures. Eng. Fract. Mech. 25, 729–737 (1986). https://doi.org/10.1016/0013-7944(86)90036-6

38. Cast3m: Finite element code developed by the CEA, (french atomic energy commission) http://www-cast3m.cea.fr/

39. Appalanaidu, Y., Roy, A., Gupta, S.: 3-D stochastic finite elements for thermal creep analysis of

piping structures with spatial material inhomogeneities. Acta Mech. 228, 3039–3062 (2017). https://doi.org/10.1007/s00707-017-1865-9

40. Norman, B., Wahren, D.: A comprehensive method for the description of mass distribution in sheets and flocculation and turbulence in suspensions. Sven. Papperstidng. 75, 807–818 (1972)

41. Matheron, G.: Variables régionalisées et leur estimation. Masson (1965)

42. Villette, F.: Damage of heterogeneous media: paper as a model material. Ph.D Thesis, Univ. Grenoble Alpes. (2020)

43. Matheron, G.: The intrinsic random functions and their applications. Appl. Probab. Trust. 5, 439–468 (1973)

44. Doube, M., Kłosowski, M.M., Arganda-carreras, I., Fabrice, P.: BoneJ : free and extensible bone image analysis in ImageJ. Bone. 47, 1076–1079 (2010). https://doi.org/10.1016/j.bone.2010.08.023.BoneJ

45. Hagman, A., Nygårds, M.: Thermographical Analysis of Paper During Tensile Testing and Comparison to Digital Image Correlation. Exp. Mech. 57, 325–339 (2017). https://doi.org/10.1007/s11340-016-0240-4

46. Rosti, J., Koivisto, J., Alava, M.: Statistics of acoustic emission in paper fracture: precursors and criticality. J. Stat. Mech. Theory Exp. 2, P02016 (2010). https://doi.org/10.1088/1742-5468/2010/02/P02016

47. Villette, F., Baroth, J., Dufour, F., Bloch, J.-F., Rolland du Roscoat, S.: Influence of material heterogeneities on crack propagation statistics using a Fiber Bundle Model. Int. J. Fract. 221, 87–100 (2020). https://doi.org/10.1007/s10704-019-00409-2